A study of porous carbon structures derived from composite of cross-linked polymers and reduced graphene oxide for supercapacitor applications

Daba T. Bakhoum [a], Kabir O. Oyedotun [a], Samba Sarr [a], Ndeye F. Sylla [a], Vusani M. Maphiri [a], Ndeye M. Ndiaye [b], Balla D. Ngom [b] and Ncholu Manyala [a*]

[a] Department of Physics, Institute of Applied Materials, SARChI Chair in Carbon Technology and Materials, University of Pretoria, Pretoria 0028, South Africa.

[b] Laboratoire de Photonique Quantique, d'Energie et de Nano-Fabrication, Faculté des Sciences et Techniques Université Cheikh Anta Diop de Dakar (UCAD) B.P. 5005 Dakar-Fann Dakar, Sénégal

*Corresponding author's email: ncholu.manyala@up.ac.za, Tel.: + (27)12 420 3549, Fax: + (27)12 420 2516

Highlights

- Porous carbons from cross-linked polymers and reduced graphene oxide is prepared via hydrothermal and activation
- A synergy of features is achieved by cross-linking of polyvinyl alcohol and polyvinyl pyrrolidone
- AC-PVA/rGO/PVP displayed high electrochemical performance
- The device recorded specific energy and power of 19.5 W h kg^{-1} and 400 W kg^{-1} respectively in 2.5 M KNO_3 electrolyte

Abstract

In this study, hydrothermal and chemical vapor deposition (CVD) methods were used to prepare cross-linked polymer-based porous carbonaceous materials designated as activated carbon from polyvinyl alcohol (AC-PVA), activated carbon from polyvinyl alcohol/reduced graphene (AC-PVA/rGO) and activated carbon from polyvinyl alcohol/reduced graphene/polyvinyl pyrrolidone (AC-PVA/rGO/PVP). The structural properties of the as-prepared samples indicated a higher degree amorphicity. The textural analysis revealed high specific surface areas along with high void fractions for the samples. The electrochemical analysis of the cross-linked polymer-based activated carbons conducted as three-electrodes revealed the samples' potential as electrode materials for supercapacitors' applications. Activated carbon from PVA/rGO/PVP exhibited a superior specific capacitance (223 F g^{-1}), a smaller charge transfer resistance (R_{CT} = 1.0 Ω) and equivalent series resistance (ESR = 0.54

Ω) as compared to AC-PVA and AC-PVA/rGO. Remarkably, a fabricated symmetric device based on the AC-PVA/rGO/PVP as electrode and designated as AC-PVA/rGO/PVP//AC-PVA/rGO/PVP, delivered a high specific energy of 19.5 W h kg^{-1} corresponding to a specific power of 400 W kg^{-1} at 0.5 A g^{-1}. Besides, the supercapacitor displayed a stable evolution of capacitance, high coulombic efficiency of 99.8% and good related capacitance retention of 82.3% during a 10 000 galvanostatic charge/discharge cycles conducted for the device in an extended cell potential of 1.6 V at 5.0 A g^{-1} in 2.5 mol L^{-1} KNO_3 aqueous electrolyte. These encouraging results demonstrate the versatile potential of the carbon materials for future electrochemical energy storage devices.

Graphical abstract

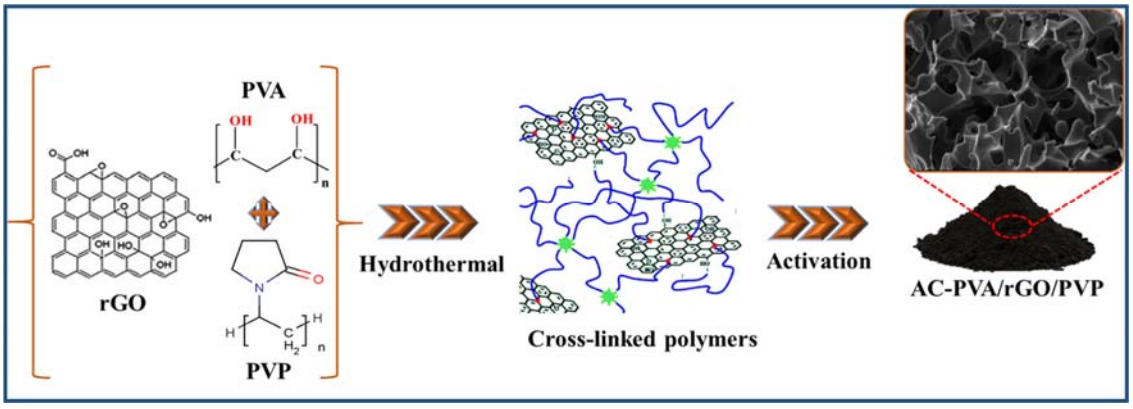

Keywords: Supercapacitor; Electrode; Polymer; Reduced graphene oxide; Composite; Activation.

Introduction

The increasing pollution of the planet due to the long-term effects of greenhouse gas emissions into the atmosphere and the finite supply of fossil fuels necessitate the implementation of alternatives to existing energy sources such as coal, oil, and/or gas [1]. Batteries and electrochemical capacitors (also known as supercapacitors) are the main technologies that can be used to store renewable energy produced by solar, water and wind [2]. Because of their

flexible power, and energy characteristics, batteries have been widely used on different scales and have been continuously studied among these electrochemical energy storage (EES) technologies [3,4]. Supercapacitors (SCs) as an alternative energy storage device are at the forefront of this research and are regarded as a specific type of device for future generation energy storage [5,6]. SCs have been widely anticipated in the energy storage sector due to their excellent cyclic stability and high specific power. As a result of the emergence of new generations of electric and hybrid vehicles, SCs have attracted huge attention as an alternative and/or complimentary device to rechargeable batteries. Therefore, it is necessary to put in more effort to improve the energy capability of SCs [7]. The development of novel porous carbon-based materials as electrodes for SCs applications can efficiently enhance the operating potential of the devices and thus improve their overall specific energy or energy density since this parameter is directly proportional to the capacitance and squared potential [8,9]. Supercapacitors are composed of two electrodes closely packed together and submerged in an electrolyte, which serves as the conducting medium between the electrodes [10]. Based on the energy storage mechanism, they are either electrochemical double-layer capacitors (EDLCs) or pseudocapacitors (PCs) [11]. The PCs are oxide- and conductive polymers-based materials owing to their high electrochemical redox reactions, which result in high values of capacity [12]. The EDLCs possess charge separation at the electrode and electrolyte interface that is responsible for the capacitance [13]. Owing to their high porosity, the EDLCs' electrodes possess a very large specific surface area and can hold even more energy per unit area, which improves the surface for charge storage thus capable of enhancing the device's electrochemical performance. Carbon materials as SCs electrodes are known for excellent characteristics such as light weight, high electrical conductivity, form, cost-effectiveness and stability [14,10] Recently, polymer-based materials have been adopted as precursors to prepare carbons and activated carbons with some of them being effectively utilized as electrodes for energy storage

devices application such as supercapacitors and batteries [15–21]. For instance, Sihao Yan *et al*. [22] synthesized a new cross-linked activated carbon nanofibers from polyacrilonitrile (PAN)/dicyandiamide (DICY) composite with nitrogen functionality, using facile and controllable way via electrospinning method for supercapacitors electrode, which exhibits a specific energy of 14.3 W h kg^{-1} corresponding to a specific power of 162.5 W kg^{-1} at a specific current of 0.5 A g^{-1} [22]. Wang *et al*. [23] considered a direct carbonization method to synthesize a nitrogen-doped porous activated carbon from polypyrrole nanowires with an good specific capacitance for supercapacitors' applications, which displayed a specific energy and specific power of 13.2 W h kg^{-1} and 257 W kg^{-1}, respectively, at a specific current of 0.33 A g^{-1} [23]. Recently, *Chuanyin et al*. [24] designed a carbonized wood cell chamber-reduced graphene oxide@PVA (CWCC-rGO@PVA) composite. Their prepared material displayed a high specific capacitance of 288 F g^{-1}, an energy density of 36 Wh kg^{-1} and a power density of 3600 W kg^{-1} at scan rates of 100 mV s^{-1} [24]. They concluded that this good electrochemical performance is correlated to the presence of rGO combining with polyvinyl alcohol (PVA). Therefore, the integration of the rGO into porous carbon is important for good electrochemical performance. This is associated to their chemical stability, good electrical conductivity, thermal stability, large surface area and the capacity to facilitate the penetration of aqueous electrolyte [25–28]. Polymer-based porous carbon materials are currently thought to be important in development of SCs for a variety of applications with the possibility to form polymer's cross- linking [29–31]. Cross-linked porous polymers such as polyvinyl alcohol (PVA), polyvinyl pyrrolidone (PVP), polyaniline (PANI) and polypyrrole (PPy) offer a great opportunity to control porous structure, surface area and adsorption properties which are crucial parameters for a good EDLC electrode [32–34]. Among the polymer-based porous carbon materials, polyvinyl alcohol (PVA) and polyvinyl pyrrolidone (PVP) have the capacity to offer a high crosslinked polymer hydrogel with dipole interaction, ionic bonds and hydrogen bonds

[35,36]. These are associated with the presence of the ldol-condensation reaction formed from OH groups in the long molecular chain PVA and further created a blending of PVP onto PVA matrix and stable -C-O-C- multi-faceted cross-linking. This cross-linking also has the potential to minimise the swelling of the PVA and the creation of more irregular interconnected pores which facilitate the diffusion of ions due to the high cross-linking density and denser packing of polymer chain promoted by the PVP [29,34–38]. Additionally, PVA and PVP are non-toxic, semi crystalline and water-soluble synthetic polymers [39,40].

In this study, we report the utilization of cross-linked PVA and PVP polymer-based precursor to prepare activated carbons via a facile two-step synthesis technique. The prepared samples characterized by using BET and SEM, reveal high specific surface areas along with high void fractions. Electrochemical analysis of the cross-linked polymer-based activated carbons conducted as three-electrodes showed the samples' potential as electrode materials for supercapacitors' applications in 2.5 mol L^{-1} KNO_3. Interestingly, the superior charge transport dynamics was recorded with the AC-PVA/rGO/PVP electrode which provide the ideal pore sizes for efficient ion transport and charge storage. The KNO_3 (K^+, NO_3^-) aqueous electrolyte has a high conductivity, non-corrosive, is environmentally friendly and cheap to synthesize [41]. Thus, AC-PVA/rGO/PVP electrode was used to fabricate a symmetric device (AC-PVA/rGO/PVP//AC-PVA/rGO/PVP) in 2.5 mol L^{-1} KNO_3. The full cell device exhibited a high specific energy of 19.5 W h kg^{-1} corresponding to a specific power of 400 W kg^{-1} at a specific current of 0.5 A g^{-1}. The device also displayed a stable evolution of capacitance, high coulombic efficiency of 99.8% and good related capacitance retention of 82.3% during a 10 000 galvanostatic charge/discharge cycles cycling test conducted in an extended cell potential of 1.6 V at 5.0 A g^{-1}. These encouraging results demonstrate the versatile potential of the carbon materials for future electrochemical energy storage devices.

2. Experimental

2.1 Synthesis of activated carbon from polyvinyl alcohol (AC-PVA)

2.1.1 Preparation of PVA powder

50 mg of PVA (molecular weight: 89000-98000, 0.1 wt%) was dispersed in 50mL of deionized (DI) water and then stirred at 80 °C until viscous (whitish-thick fluid). The recovered mixture was taken through a hydrothermal process using a Teflon-lined autoclave at 180 °C for a period 14 h as shown in scheme 1(a). The obtained solid sample (PVA powder) was washed with DI water until neutral pH and dried overnight at 60 °C in an electric oven.

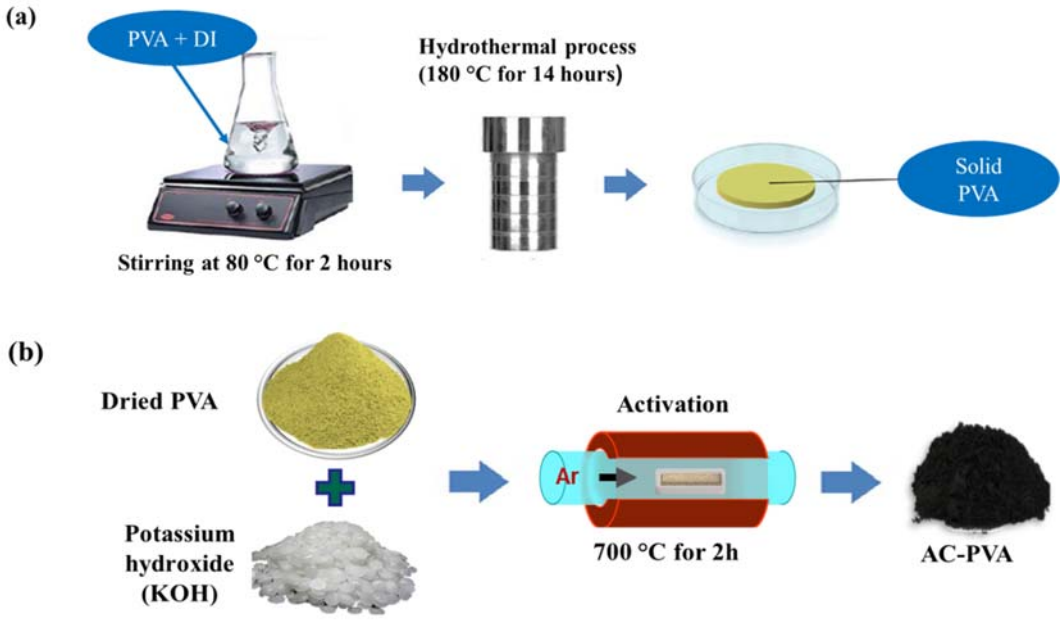

Scheme 1. Schematic of the synthesis route of (a) the dried polyvinyl alcohol (PVA) and (b) activated carbon from polyvinyl alcohol (AC-PVA) samples.

2.1.2 Preparation of activated carbon from polyvinyl alcohol (AC-PVA)

The activated carbon from polyvinyl alcohol (AC-PVA) was obtained by one step of activation process. The dried PVA powder was activated at 700 ˚C (at a ramping rate of 5 ˚C min^{-1}) in 300 sccm flow of argon gas for 2 h using KOH as the activating agent in ratio 1(PVA):2(KOH)

as depicted in scheme 1(b). The obtained product (AC-PVA) was severally washed with DI water and then dried at 60 °C overnight.

2.2 Synthesis of activated carbon from polyvinyl alcohol and reduced graphene oxide (AC-PVA/rGO) sample

2.2.1 Synthesis of rGO

The reduced graphene oxide (rGO) adopted in this study was synthesized at room temperature using a modified Hummers method already reported [42]. In the synthesis process, 1.0 g of graphite powder and 6.0 g of $KMnO_4$ were put together in a beaker containing 120 mL of concentrated sulphuric acid (H_2SO_4) (95-99.9%). The mixture was stirred for 15 min to secure a homogeneous dispersion of the solution. This was then transferred into a silicone oil bath and further stirred at 50 °C for 180 min. The obtained thick dark-grey solution was left to cool down to room temperature. A stoichiometric volume of 30% H_2O_2 and distilled water was subsequently poured into the solution to subdue residual permanganate and manganese (IV) oxide mixture to a colourless soluble manganese sulphate. The reacted solution was then stirred for 1 min and then centrifuged for 10 min with the supernatant decanted away. The recovered gelatinous solution was re-dispersed in distilled water by mechanical shaking (250 oscillations/minute) for 1 h to reduce the graphene oxide sample, with additional centrifugation for 30 min. The recovered solid (reduced graphene oxide) was dried overnight in an electric furnace under normal pressure at a temperature of 90 °C.

2.2.2 Preparation of polyvinyl alcohol and reduced graphene oxide (PVA/rGO)

50 mg of rGO was first dispersed in 50 ml of DI water and then added with 50 mL of PVA. Thereafter, the procedure adopted in preparation of PVA (see section 2.1.1) was repeated to obtain the dried PVA/rGO.

2.2.3 Preparation of activated carbon from polyvinyl alcohol/reduced graphene (AC-PVA/rGO) sample

The obtained dried PVA/rGO sample was mixed with KOH in ratio 1(PVA/rGO):2(KOH) then activated by following the procedure already stated in section 2.1.2 (scheme 1 (b)).

2.3 Synthesis of activated carbon from polyvinyl alcohol/reduced graphene/polyvinyl pyrrolidone (AC-PVA/rGO/PVP) materials

2.3.1 Preparation of PVA/rGO sample

50 mg of rGO was first dispersed in 50 mL of DI water and then added with 50 mg of PVP (molecular weight: 10 000). The mixture was stirred to obtain homogenous solution and was later added into 50 mL of the viscous mixture of PVA/water. Thereafter, the procedure adopted in section 2.1.1 was repeated to obtain the PVA/rGO powder material.

2.3.2. Preparation of AC-PVA/rGO/PVP prepared materials

The dried PVA/rGO/PVP material was activated using KOH in a ratio 1(PVA/rGO/PVP):2(KOH) following the procedure already described in section 2.1.2 (scheme 1 (b)).

2.2 Material characterization

The structural analysis of the as-prepared nanomaterials was studied by using a Bruker BV 2D PHASER Best Benchtop (PANalytical BV, Amsterdam, Netherland) equipment operating with $CuK_{\alpha 1}$ (λ=0.15406 nm) source at 30 mA and 50 kV with $\theta/2\theta$ reflection geometry in the range from 5-90 ° and in a step size of 0.005 °. Raman spectroscopy analysis of the materials was carried out with the aid of a WITec alpha 300 RAS+ Confocal micro-Raman microscope (Focus Innovations, Ulm, Germany) with the laser wavelength set at 532 nm over a 180 s spectral acquisition time and laser power of 5 mW 532 nm. A Zeiss Ultra plus 55 field emission scanning electron microscope (FE-SEM) (Akishima, Japan) operated at a potential of 2.0 kV

and equipped with energy dispersive X-ray (EDX) device was used to investigate the samples' morphology and elemental compositions. In order to analyse the porous structure of as prepared materials, a Quantachrome (NOVA touch NT 2LX-1, Volts 220 USA) operated with the Quantachrome TouchWin Software Version: 1.22 was used with a Brunauer–Emmett–Teller (BET) technique. The N_2-absorption/desorption isotherms and the specific surface area values of the materials were obtained by using the adsorption branch in the relative pressure range (P/P_0) of 0.05 - 0.95. The specific surface area values were calculated in the relative pressure range of 0.05 - 0.3. The pore size distribution (PSD) of the samples was determined by the density functional theory (DFT) method. Before the measurements, the samples were degassed at 150 °C for 12 h under vacuum.

2.3 Electrochemical characterization

For the fabrication of electrodes, 80 wt.% of active material, 10 wt.% of conductive carbon acetylene black and 10 wt.% polyvinylidene difluoride (PVDF) as a binder were homogenized and dispersed in 1-methyl-2- pyrrolidinone (NMP) to make a slurry using an agate pestle/mortar. The resulting mixture was uniformly pasted on a 1 cm^2 nickel foam (NF) support and dried overnight at 60 °C to ensure complete evaporation of the solvent. The loading mass of active materials was determined to be ~ 2.5 mg cm^{-2} for all the samples. Electrochemical measurements of the electrodes performed by using a 16-channel Biologic VMP-300 potentiostat (Knoxville TN37,930, USA) controlled by the EC-Lab V11.33 software at room temperature, were carried out in a three-electrode system using the 3 M KCl saturated Ag/AgCl and glassy carbon as reference electrode (RE) and counter electrode (CE), respectively. The three-electrode measurements were initially performed to understand the charge storage mechanism of the materials in 2.5 M KNO_3 aqueous solution in a reverse potential range of 0–0.8 V and - 0.8–0 V vs Ag/AgCl, respectively, for both the cyclic voltammetry (CV) galvanostatic charge/discharge (GCD) tests conducted on the samples. Different

electrochemical properties such as CV, GCD, electrochemical impedance spectroscopy (EIS) and cycling stability tests were carried out on the as-prepared materials. The CV test was done at different scan rates ranging from 10 mV s^{-1} to 100 mV s^{-1} while the galvanostatic GCD analysis was carried out at different current densities from 0.5 A g^{-1} to 10 A g^{-1}. The EIS was conducted in an open circuit potential at a frequency range of 10 mHz - 100 kHz.

The specific capacitance C_{sp} of the as-prepared single half-cell electrode was calculated by using the formula stated in equation (1) [43]:

$$C_{sp} = \frac{I\Delta t}{m\Delta V} \quad (\text{F g}^{-1}) \tag{1}$$

Where I (mA) is the charge/discharge current, $\Delta V(V)$corresponds to operating potential window, $\Delta t(s)$ is the discharge time, m (mg) represents the amount of active material electrodes.

The specific capacitance C_s for the symmetric device is given by the equation below using the total mass m_T (mg) [44,45].

$$C_s = \frac{I\Delta t}{m_T\Delta V} \quad (\text{F g}^{-1}) \tag{2}$$

The specific energy and specific power were evaluated through the discharge profiles by using equations (3 and 4) [45].

$$E_d = \frac{C_s\Delta V^2}{7.2} \quad (\text{W h kg}^{-1}) \tag{3}$$

$$P_d = 3600\frac{E_d}{\Delta t} \quad (\text{W kg}^{-1}) \tag{4}$$

where E_d and P_d are the specific energy and specific power, respectively.

The columbic efficiency, C_E was assessed over the cell potential by using the following equation (5) from the GCD curves [46].

$$C_E = \frac{t_D}{t_C} \times 100 \quad (5)$$

Where t_D and t_C stand discharge and charge time, respectively.

3. Results and discussion

3.1 Structural, textural and morphological characterization

Fig. 1 shows the XRD patterns of the as-prepared carbon samples. The X-ray diffraction analysis reveals comparable patterns for all the as-prepared samples, showing peaks associated with graphite materials.

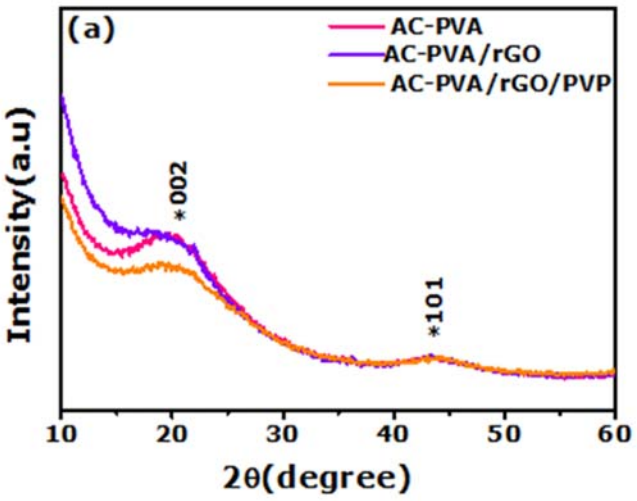

Fig. 1. XRD patterns of AC-PVA, AC-PVA/rGO and AC-PVA/rGO/PVP composites.

The analysis revealed all samples are amorphous in nature, showing diffraction peaks at around 2θ = 22 º and 45 º that are ascribed to characteristic (0 0 2) and (1 0 1) planes of carbon, respectively, with JCPDS number: 41-1487 [10].

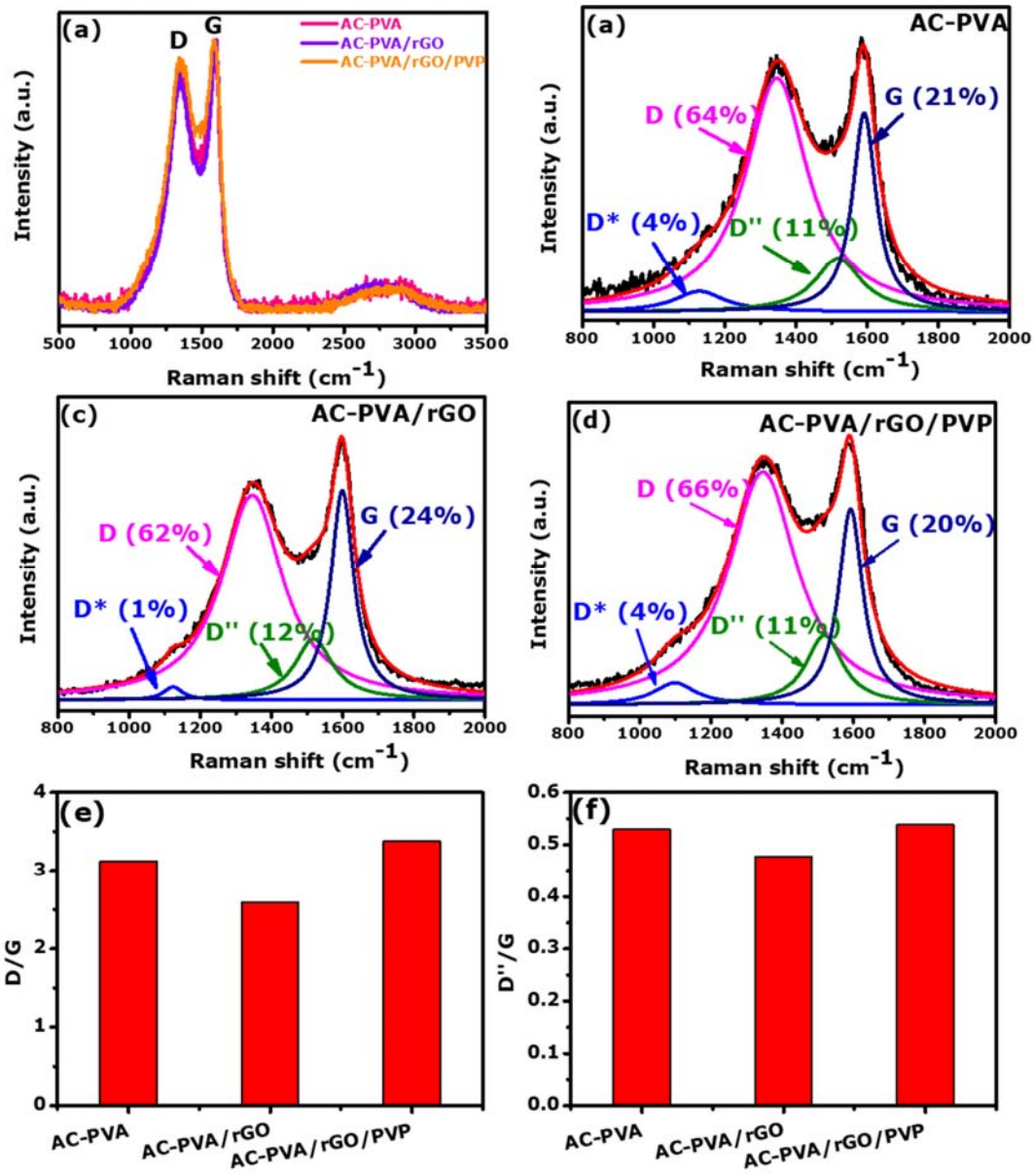

Fig. 2. (a) Raman spectra, (b-d) Raman spectra deconvolution for AC-PVA, AC-PVA/rGO and AC-PVA/rGO/PVP composites, respectively, (e) plot of ratio of D to G, and (f) plot of ratio of D" to G for AC-PVA, AC-PVA/rGO and AC-PVA/rGO/PVP composites, respectively.

For the study of textural defects in carbon materials, Raman Spectroscopy has remained one of the most important procedures [47]. Fig. 2(a) is the representative Raman analysis of as-synthesized polymer-based activated carbon materials, while Fig. 2(b-d) reveals the deconvoluted Raman spectra analysis of the activated carbon samples. For all the prepared

materials, the analysis shows two prominent peaks at 1337 cm^{-1} (D band) and 1590 cm^{-1} (G band). The noticed peak at 1337 cm^{-1} is a characteristic of disordered graphite structure and corresponds to the C–C graphitic lattice vibration mode with A_{1g} symmetry. In the presence of defects, the D-peak could be due to the breathing modes of sp^2 rings being triggered by a dual resonance effect [48]. The observed peak at 1590 cm^{-1} is a result of the in-plane stretching phonon mode of C-C bond in the graphitized carbon materials [10]. A broad peak in their range of 2400-3300 cm^{-1} was observed in all prepared samples. The hump can be attributed to the amalgamation for several overtone peaks; 2D*, 2D, D+G and 2D' [49,50].

The deconvoluted peaks (Fig. 2(b-d)) were done to examine the different vibrational modes of the activated carbon material in greater details, using Lorentzian curve fittings of the various combinations in accordance with previously published similar materials from the literature [51]. In addition, the deconvolution was also used to obtain the integral areas of the D and G peaks, which were then used to determine the D/G ratio of the disordered carbon (D) relative to graphitic carbon [52]. The origin of D" band is linked to the amorphous carbon and the lattice vibrations referred to as sp^2-sp^3 bonds trigger the D* band [53,54]. Fig. 2(e) displays the plot of (I_D/I_G) ratio as function of the carbon materials. The estimated I_D/I_G are 3.12, 2.60, and 3.37 for AC-PVA, AC-PVA-rGO, and AC-PVA/rGO/PVP samples, respectively, confirming the high ratio disordered nature of the as-prepared samples [55]. AC-PVA/rGO/PVP composite exhibits higher I_D/I_G values compared to others samples. Analogously, Fig. 2(f) shows the plot of the D"/G ratio as a function of AC-PVA, AC-PVA/rGO and AC-PVA/rGO/PVP composites which revealed a higher ratio of amorphous carbon (D") relative to the graphitic carbon (G). The higher ratio of disorder (D) and amorphous carbon (D") relative to the graphitic carbon (G) attributed to AC-PVA/rGO/PVP as compared to the others materials (AC-PVA and AC-PVA-rGO) might allow a good wettability and more active sites, resulting in good the electrochemical performance [41,56].

Nitrogen gas adsorption/desorption process was performed to analyze the textural properties of the obtained materials. Fig. (3) shows N_2 adsorption-desorption isotherms and the pore size distribution of the AC-PVA, AC-PVA/rGO and AC-PVA/rGO/PVP samples. The isotherm curves as observed in Fig. 3(a) depicted a type I with an H4 hysteresis loop behaviour according to IUPAC classification [31,57,58]. This indicates that all the synthesized porous carbon materials are mainly composed of micropores with the presence of mesopores and can provide continuous ion-transfer channels [59]. At a low relative pressure range, the appearance of the knee indicated an abundant presence of micropores that are responsible for the charge storage and ions adsorption [60–62]. Moreover, the slope at medium pressure and the weak hysteresis loop at high pressure range, are reflecting the existence of mesopores which generate pathways for ions throughout their movement from the electrolyte to the in electrode /electrolyte interface [46].

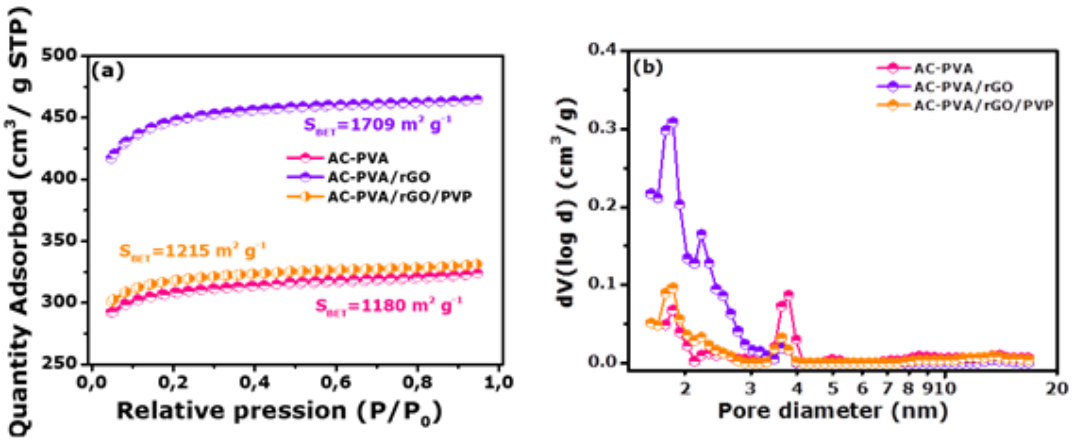

Fig. 3. (a) N_2 adsorption/desorption and (b) pore-size distribution of the samples.

The BET specific surface area (SSA), porosity data of the AC-PVA, AC-PVA/rGO and AC-PVA/rGO/PVP composites are summarized in Table 1. The SSA of AC-PVA sample (1180 m^2 g^{-1}) increased with the addition of rGO (1709 m^2 g^{-1}). However, a decrease of the AC-PVA/rGO/PVP surface area (1215 m^2 g^{-1}) is noticed with the addition of PVP in the AC-PVA/rGO composite. The same trend is observed for the total pore volume and micropore

volume in the activated carbon samples. The diminution of the SSA and porosity of the AC-PVA/rGO/PVP composite could be due to the interaction of PVP with the surface sites that might block or clog some pores of the carbon matrix [63–66]. Recently, Tie *et al.*[66] have demonstrated that the SSA of the porous carbon could be reduced depending on the content of PVP. This is related to the low utilization of pore space [66]. The pore size distribution plots obtained by Density Functional Theory (DFT) method is shown in Fig. 3(b) and confirms the existence of both micropores (below 2 nm) and the mesopores (above 2 nm) [67]. The presence of hierarchically porous structures can significantly improve the diffusion and mobility of electrolyte ions, leading to an increase in specific capacitance and rate capability of carbon based-electrodes for supercapacitors [68]. Due to physical charge accumulation at the electrolyte/porous carbon interface, electrical double layers usually form, so a large surface area becomes essential [62].

Table 1. BET analysis of as-synthesized carbon samples.

Samples	**Textural properties**		
	BET SSA ($m^2 g^{-1}$)	Total pore volume ($cm^3 g^{-1}$)	Micropore volume ($cm^3 g^{-1}$)
AC-PVA	1180	0.50	0.46
AC-PVA/rGO	1709	0.72	0.66
AC-PVA/rGO/PVP	1215	0.51	0.47

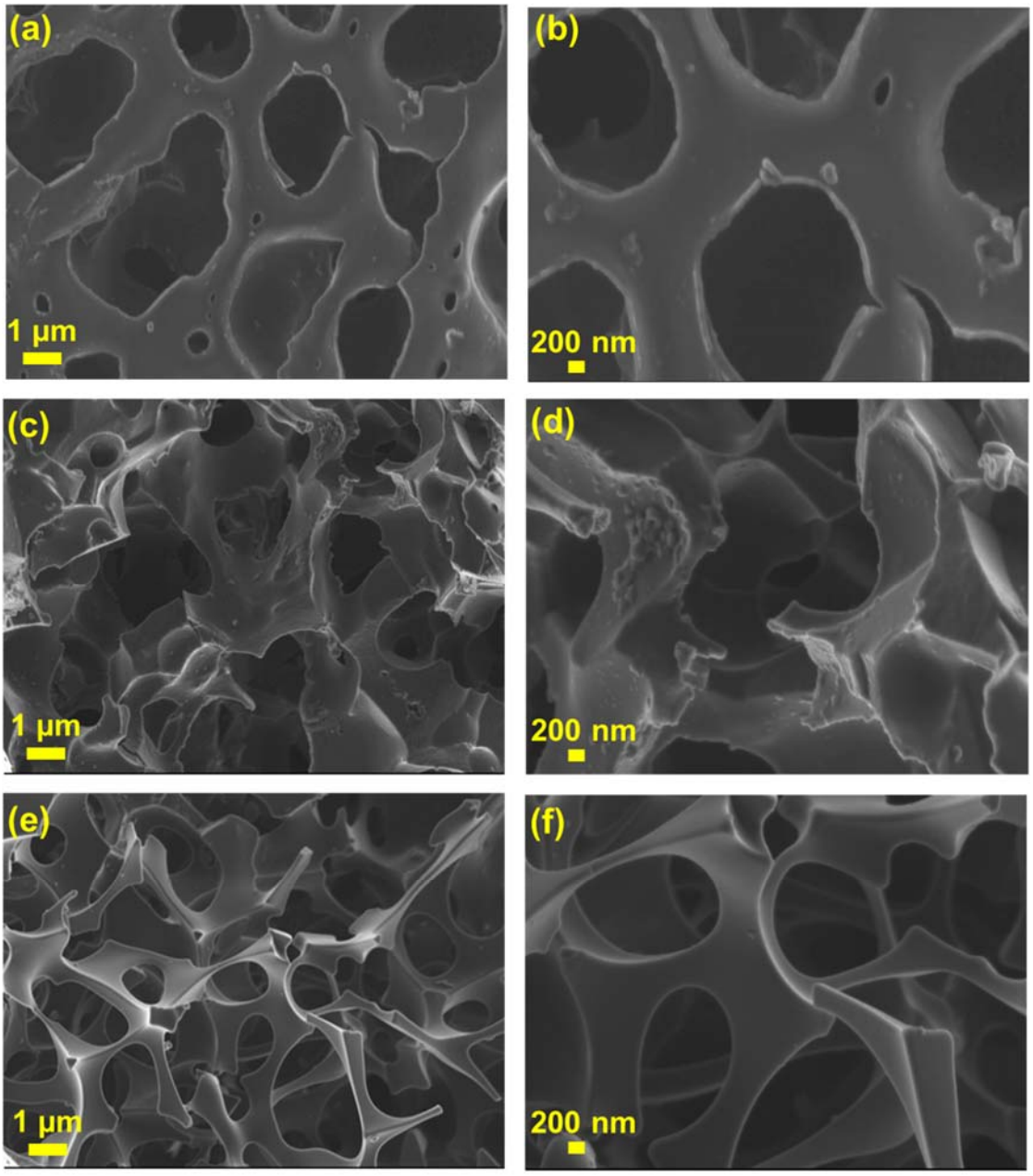

Fig. 4. SEM micrographs at low and high magnification of (a-b) AC-PVA, (c-d) AC-PVA/rGO and (e-f) AC-PVA/rGO/PVP composites.

Scanning electron microscope (SEM) is a very important technique to analyze and examine the morphological features of as-prepared materials**.** Fig. 4 shows SEM images of AC-PVA, AC-PVA/rGO and AC-PVA/rGO/PVP samples at low and high magnification scales. All activated

carbons exhibited similar porous framework morphology with irregular interconnecting channels. It can be observed that the AC-PVA/rGO/PVP presents greater interconnected porous network than the other samples due to the crosslinking process which creates channels for the transport of charge carriers and could improve the electrochemical properties of the polymer activated carbon [32,36,69].

The creation of a highly porous network on the structure of the as-prepared carbon materials can be correlated to the potassium hydroxide (KOH) activation which releases carbon monoxide (CO) and carbon dioxide (CO_2) gases upon the reaction of KOH and carbon [67]. The activation process is described as following: [70]

$$6\,KOH + 2\,C \rightarrow 2\,K + 3\,H_2 + 2\,K_2CO_3 \quad (1)$$

The decomposition of the KOH generates potassium bicarbonate, metallic potassium and hydrogen gas. At elevated temperatures (>700 °C) the decomposition of the potassium bicarbonate produces CO_2 and CO gases which promotes further pores through carbon gasification [71].

The production of the pores increases the surface area and pore volume of the activated carbon, optimizing the electrochemical properties for better energy storage. The carbon framework has varying porosity, which might help on the ion-accessible surfaces for rapid ion transport in high performing supercapacitors [72,73].

Fig. 5(a-c) shows the EDX elemental composition of the samples with their respective elemental wt. %, indicating the expected carbon and oxygen. All the carbon materials display an elevated amount of carbon in the range of 85-92 wt. % and oxygen content (7 to 15 wt. %). The addition of rGO and PVP into AC-PVA results to the increase of carbon content but reduce the oxygen content into the AC-PVA/rGO and AC-PVA/rGO/PVP composites. The activated carbon from PVA/rGO/PVP exhibits the highest carbon content than the other prepared

samples. Fig. 6 represents the elemental mapping of the various activated carbon materials analyzed by using energy dispersive X-ray (EDX) mappings. Fig. 6(a-c) shows the mutual elemental map of the samples with respective individual elemental map of C and O, respectively. The revealed maps indicated a homogeneous distribution of the elements within sample.

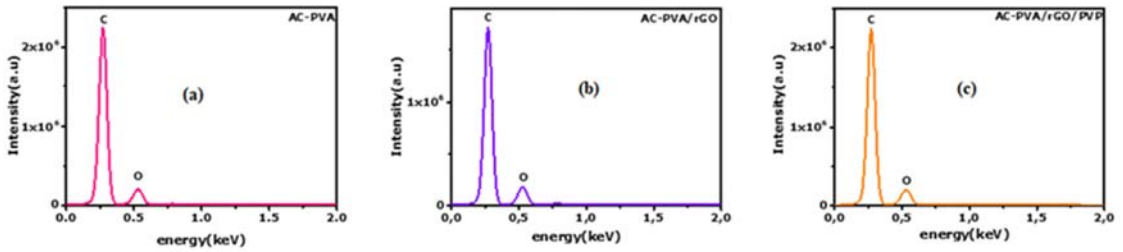

Element	Weight(%)
Carbon(C)	85.3
Oxygen(O)	14.7

Element	Weight(%)
Carbon(C)	87.8
Oxygen(O)	12.2

Element	Weight(%)
Carbon(C)	92.1
Oxygen(O)	7.9

Fig. 5. EDS spectra of (a) AC-PVA, (b) AC-PVA/rGO and (c) AC-PVA/rGO/PVP composites.

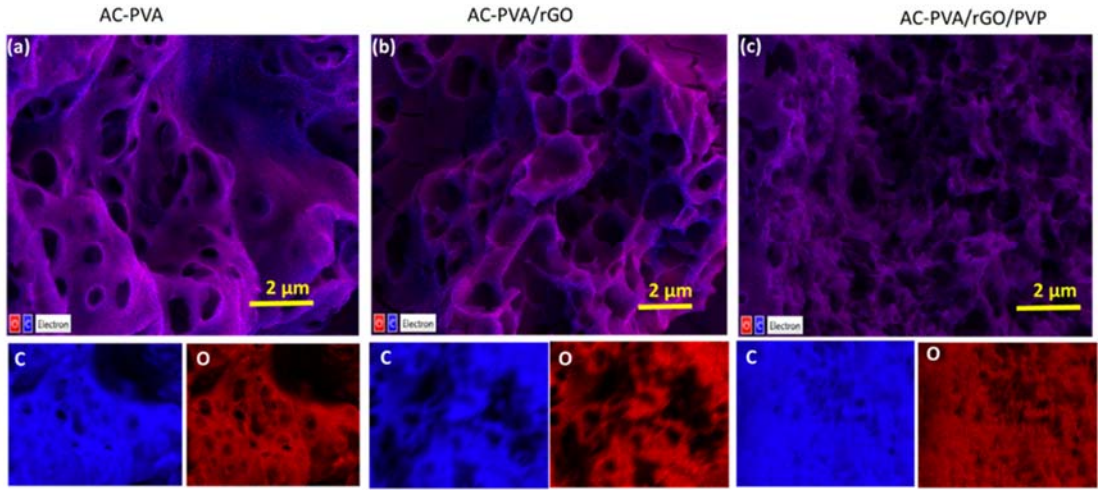

Fig. 6. EDS mapping of AC-PVA, AC-PVA/rGO and AC-PVA/rGO/PVP composites, respectively.

2.3.2. Three-electrode electrochemical evaluations of AC-PVA, AC-PVA/rGO and AC-PVA/rGO/PVP

Electrochemical properties of the as-synthesized electrode materials were investigated via a three-electrode configuration using 2.5 M KNO_3 solution as the electrolyte. Fig. 7(a-b) shows the comparative cyclic voltammogram (CV) plots of as-prepared nanomaterials at a scan rate of 50 mV s^{-1} in the negative (-0.80 to 0 V) and positive (0 to 0.80 V) potential, respectively. All the CV curves present the quasi-rectangular behaviour, which is typical of EDLC materials. The AC-PVA/rGO/PVP composite is observed to exhibit a higher current response compared to others. Fig. S1(a-b) in the supporting information represents the galvanostatic charge-discharge (GCD) curve of the samples in a reverse potential at a specific current of 1 A g^{-1}, respectively. However, the AC-PVA/rGO/PVP composite shows a longer discharge time compared to AC-PVA and AC-PVA/rGO samples. The indicated values of specific capacitance in Fig. 7(c-d) were estimated via the full GCD curves of all samples as shown in Fig. S2, Fig. S3 *(see supporting information)* and Fig. 8(c-d) for AC-PVA, AC-PVA/rGO and AC-PVA/rGO/PVP samples, respectively.

The AC-PVA/rGO/PVP electrode shows a better performance compared to the other samples according to Fig. 7(a-b) and S1 *(see the supporting information)*. The AC-PVA/rGO/PVP composite is observed to exhibit a higher specific capacitance as shown in Fig. 7(c-d), resulting from the significant impact of the rGO and PVP incorporated in the AC-PVA material. This may be explained by the fact that micropore feature created by crosslinking makes easier for electrolytes to make contact with the internal polymer backbone and promote the redox reaction [35].

Electrochemical results of the AC-PVA/rGO/PVP show that the unique cross-linked structures aid to increase electron transport as well as conductivity and wettability, resulting in a lower internal resistance and an apparent promotion of rate capability [22,35].

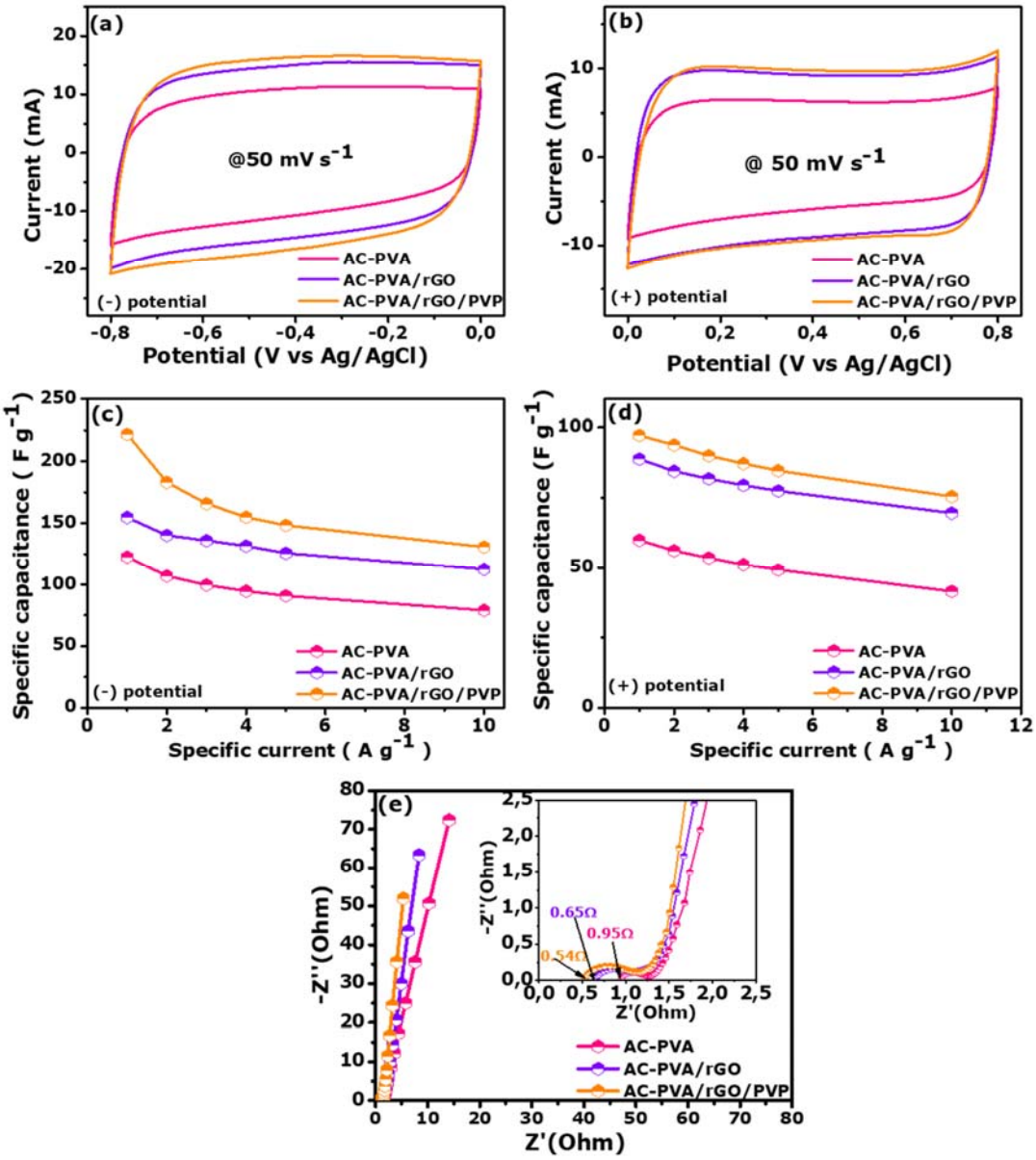

Fig. 7. (a- b) CV curves, (c-d) specific capacitance against specific current in the reverse potential and (e) Nyquist impedance plots of all the AC electrodes.

Fig. 7(e) depicted a Nyquist plot with the inset showing equivalent series resistance (ESR) and resistance charge transfer (R_{CT}) for different as-prepared electrodes. The AC-PVA/rGO/PVP electrode has the lowest ESR (0.54 Ω) and the smallest R_{CT} (1.0 Ω) as compared to AC-PVA (ESR = 0.95 Ω, R_{CT} = 1.25 Ω) and AC-PVA/rGO (ESR = 0.65 Ω, R_{CT} = 1.10 Ω). The AC-

PVA/rGO/PVP electrode displays as well a shorter diffusion length, and is closer to the ideal vertical line (Z"-axis). These low ESR and R_{CT} values for AC-PVA/rGO/PVP is attributed to excellent ion diffusion at the electrode–electrolyte interface alongside less resistance between the electrode material and current collector [67].

Based on the superior capacitive response of the AC-PVA/rGO/PVP material a complete electrochemical evaluation was performed. Fig. S4 in the supporting information displays the GCD cycling test analysis of the as-prepared samples electrodes conducted at a specific current of 10 A g^{-1} for up to 5000 cycles. From the Fig. S4(c), the AC-PVA/rGO/PVP electrode showed a better stability in terms of both capacitance retention of 99.3% and coulombic efficiency (100%) as compared to AC-PVA and AC-PVA/rGO electrodes. It is associated to a high electronic conductivity owing to its low ESR and R_{CT} values (0.51 Ω and 1.0 Ω) as seen in Fig. 7(e). Besides, the incorporation of carbon nanomaterials induces surface dependent capacitance dominated process, which is dependent on the carbon surface area and electronic conductivity [10].

Fig. 8(a-b) depicted the full CV curves of AC-PVA/rGO/PVP electrode in the reverse potentials with its corresponding GCD curves as displayed in Fig. 8(c-d) at distinct scan rates and specific currents ranging from 5 to 100 mV s^{-1} and 1 to 10 A g^{-1}, respectively.

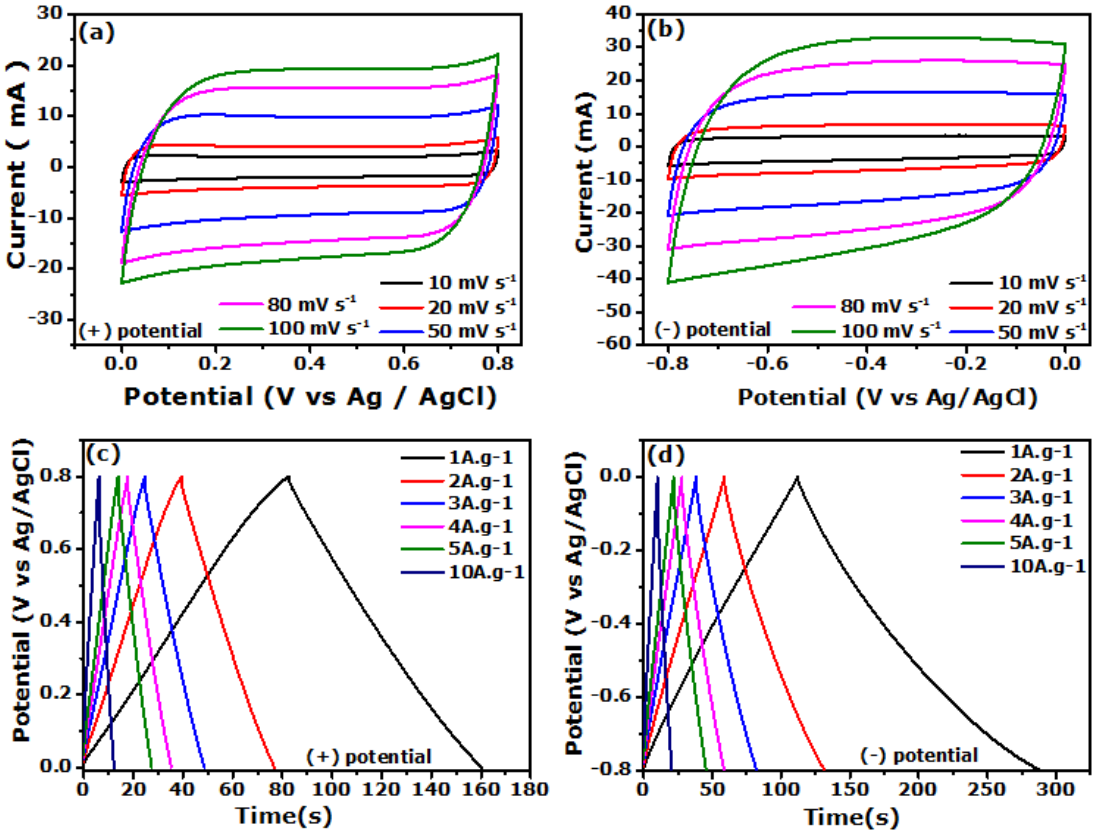

Fig. 8. (a-b) complete CV curves and (c- d) GCD curves of AC-PVA/rGO/PVP in both negative and positive potentials.

All the CV curves showed similar shapes, with the current response found to rise as the scan rate increased from 5 to 100 mV s^{-1}, indicating that the fast charge-discharge process is reversible. Both the CV profiles and GCD curves display the EDLCs materials' signature. The sample's less distorted CV and GCD curves indicate quick ion diffusion kinetics as well as current response on potential reversal [10]. The specific capacitance of the AC-PVA/rGO/PVP estimated the GCD curves (as shown in figure 7 (c- d)) in both positive and negative potential windows at different specific currents ranging from 1 to 10 A g^{-1} via the 3-electrode measurements were found to be 100 and 223 F g^{-1} in both positive and negative potential windows, respectively, compared to (50 and 123) and (93 and 187) F g^{-1} for AC-PVA and AC-PVA/rGO electrodes at the same specific current of 1 A g^{-1}, respectively.

2.3.3. Electrochemical evaluations of symmetric AC-PVA/rGO/PVP//AC-PVA/rGO/PVP device

Based on electrochemical performance of the AC-PVA/rGO/PVP electrode, a symmetric device designated as AC-PVA/rGO/PVP//AC-PVA/rGO/PVP was fabricated to further explore the performance of the material using the same 2.5 M KNO_3 electrolyte. Fig. 9(a) and (b) depict the CV and GCD profiles of the symmetric cell recorded at a scan rate and a specific current ranging from 10 to 100 mV s^{-1} and 0.5 to 10 A g^{-1}, respectively, in a wider working potential of 1.6 V.

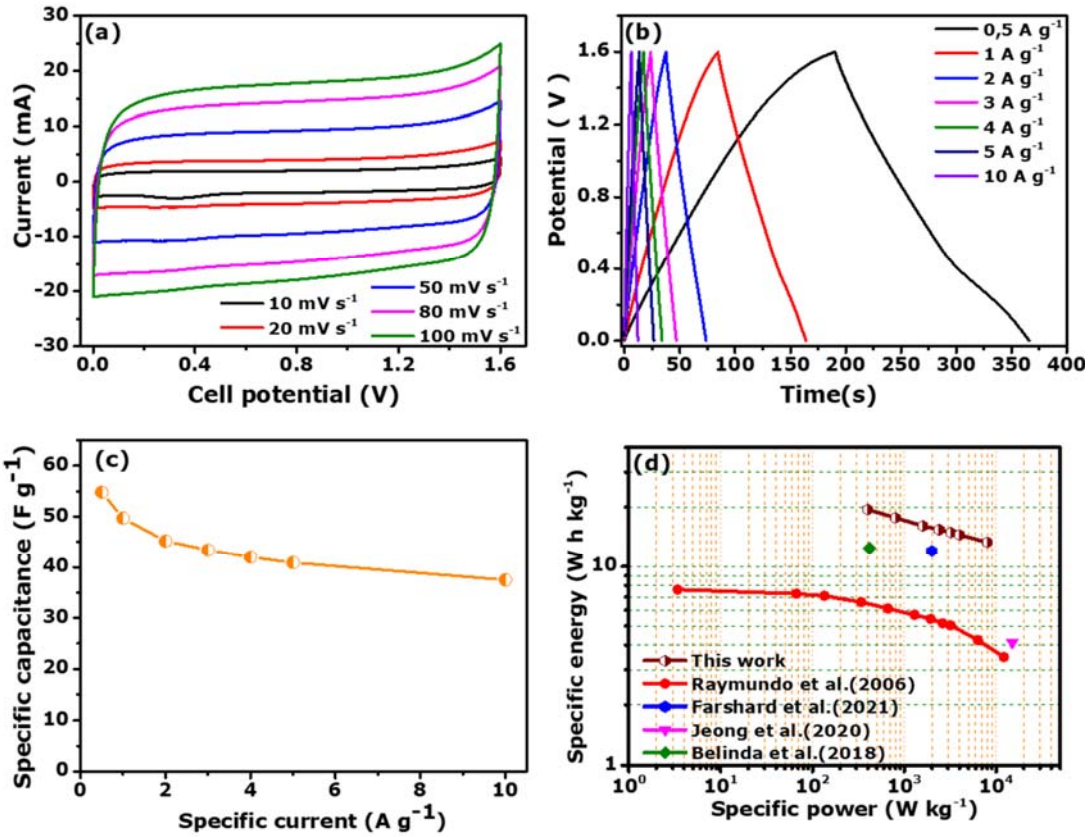

Fig. 9. (a) CV curves at different scan rates, (b) GCD curves at different specific currents, (c) specific capacitance against specific currents and (d) Ragone plot of the AC-PVA/rGO/PVP //AC-PVA/rGO/PVP symmetric device, respectively.

The symmetric device's specific capacitances estimated at distinct specific currents according to Eq. (2) are plotted as a function of specific current in Fig. 9(c). The device gave a maximum specific capacitance of about 54.8 F g^{-1} at 0.5 A g^{-1}, corresponding to a satisfying specific energy and specific power of 19.5 W h kg^{-1} and 400 W kg^{-1}, respectively, as shown in Fig. 9(d). Furthermore, the specific energy remained at 13.3 W h kg^{-1} with a specific power of 8 kW kg^{-1}, even at high specific current of 10 A g^{-1}. These values of the specific energy and specific power for the AC-PVA/rGO/PVP//AC-PVA/rGO/PVP device outperform those recently reported values in the literature on activated carbon derived from polymers as shown in Fig. 9(d) such us AC-PPY-6//AC-PPY-6 [74] , PVA + PVP + graphene-base// PVA + PVP + graphene-base [34], PHCNF30// PHCNF30 [43], ALG-C// ALG-C [16].

Fig. 10(a) is a plot showing both capacitance retention and coulombic efficiency for the device against cycle numbers. The symmetric supercapacitor revealed an excellent coulombic efficiency of ~ 100% for over 10,000 GCD cycles and a capacitance retention of about 82.3 % at a specific current of 10 A g^{-1}, which indicates the device did not experience any remarkable structural defect throughout the long cycling test. This unique behavior is attributed to the remarkable nanopores and irregular interconnecting channels of the AC-PVA/rGO/PVP electrode, which can accelerate a swift charge transport mechanism [42,75]. The good stability of the electrode materials is due to the influence of the unique cross-linked structures between the two polymers [22,76].

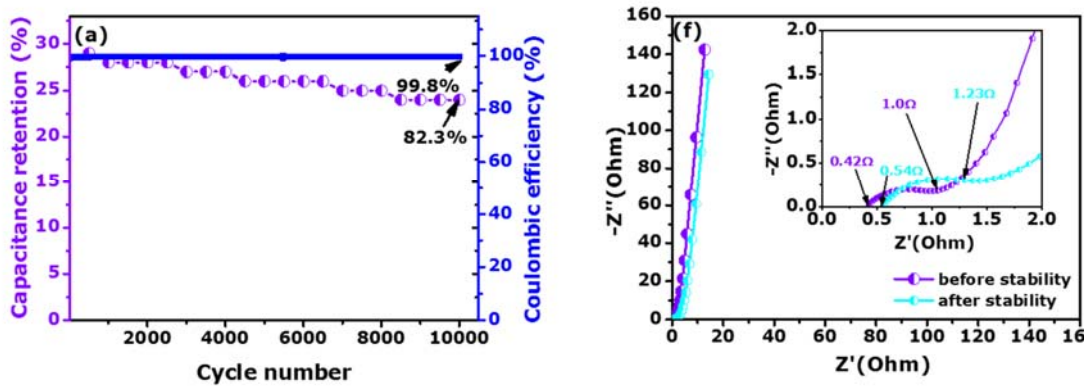

Fig. 10. (a) Columbic efficiency and specific capacitance retention against cycle number and (b) Nyquist plots before and after cycling test for the AC-PVA/rGO/PVP //AC-PVA/rGO/PVP symmetric device.

Fig. 10(b) exhibits the Nyquist plots of the symmetric device before and after 10,000 cycling test which present in low frequency a quasi-linear vertical paralleled to -Z" axis. At high frequency (inset of the Fig. 10(b)), the ESR and R_{CT} values of the AC-PVA/rGO/PVP//AC-PVA/rGO/PVP device slightly increased from 0.42 Ω before cycling to 0.54 Ω and from 1 Ω to 1.3 Ω after 10,000 cycling test, respectively.

Conclusion

Cross-linked polymer-based activated carbon electrode materials were successfully synthesized via a simple and efficient hydrothermal and chemical vapour deposition (CVD) techniques. Electrochemical evaluations of the cross-linked polymer-based activated carbon materials conducted as three-electrode showed the samples' potential as electrode for supercapacitors' applications. A fabricated symmetric supercapacitor designated as AC-PVA/rGO/PVP//AC-PVA/rGO/PVP, based on the AC-PVA/rGO/PVP as both positive and negative electrodes could deliver a high specific energy of 19.5 W h kg^{-1} corresponding to a specific power of 400 W kg^{-1} at a specific current of 0.5 A g^{-1}.

The device also displayed a stable evolution of capacitance, high coulombic efficiency and good related capacitance retention energy during a 10,000 GCD cycles cycling test conducted in an extended cell potential of 1.6 V at 10 A g^{-1} in 2.5 mol L^{-1} KNO_3 solution. These encouraging results demonstrate the versatile potential of the polymer derived activated carbon for future electrochemical energy storage devices.

Acknowledgements This study is supported by the South African Research Chairs Initiative of the Department of Science and Technology and National Research Foundation of South Africa (Grant No. 61056). The opinion, finding, and conclusion specified in this work are those of the author(s), and the NRF is not in any form accountable in this regard. D. T. Bakhoum appreciates financial support from the Organization for Women in Science for the Developing World (OWSD) and Swedish International Development Cooperation Agency (Sida), NRF through SARChI in Carbon Technology and Materials and the University of Pretoria.

References

[1] L. Borchardt, M. Oschatz, S. Kaskel, Tailoring porosity in carbon materials for supercapacitor applications, Mater. Horizons. 1 (2014) 157–168. https://doi.org/10.1039/c3mh00112a.

[2] S. Maddukuri, D. Malka, M.S. Chae, Y. Elias, S. Luski, D. Aurbach, On the challenge of large energy storage by electrochemical devices, Electrochim. Acta. 354 (2020) 136771. https://doi.org/10.1016/j.electacta.2020.136771.

[3] D. Kundu, E. Talaie, V. Duffort, L.F. Nazar, The emerging chemistry of sodium ion batteries for electrochemical energy storage, Angew. Chemie Int. Ed. 54 (2015) 3431–3448. https://doi.org/10.1002/anie.201410376.

[4] S. Zhang, N. Pan, Supercapacitors performance evaluation, Adv. Energy Mater. 5 (2015) 1401401. https://doi.org/10.1002/aenm.201401401.

[5] S. Liu, L. Wei, H. Wang, Review on reliability of supercapacitors in energy storage applications, Appl. Energy. 278 (2020) 115436.

https://doi.org/10.1016/j.apenergy.2020.115436.

[6] K.V.G. Raghavendra, R. Vinoth, K. Zeb, C.V.V. Muralee Gopi, S. Sambasivam, M.R. Kummara, I.M. Obaidat, H.J. Kim, An intuitive review of supercapacitors with recent progress and novel device applications, J. Energy Storage. 31 (2020) 101652. https://doi.org/10.1016/j.est.2020.101652.

[7] A.A. Mirghni, K.O. Oyedotun, B.A. Mahmoud, A. Bello, S.C. Ray, N. Manyala, Nickel-cobalt phosphate/graphene foam as enhanced electrode for hybrid supercapacitor, Compos. Part B Eng. 174 (2019) 106953. https://doi.org/10.1016/j.compositesb.2019.106953.

[8] Z. Fan, J. Yan, T. Wei, L. Zhi, G. Ning, T. Li, F. Wei, Asymmetric supercapacitors based on graphene/MnO_2 and activated carbon nanofiber electrodes with high power and energy density, Adv. Funct. Mater. 21 (2011) 2366–2375. https://doi.org/10.1002/adfm.201100058.

[9] H. Zhang, L. Lin, B. Wu, N. Hu, Vertical carbon skeleton introduced three-dimensional MnO_2 nanostructured composite electrodes for high-performance asymmetric supercapacitors, J. Power Sources. 476 (2020) 228527. https://doi.org/10.1016/j.jpowsour.2020.228527.

[10] K.O. Oyedotun, F. Barzegar, A.A. Mirghni, A.A. Khaleed, T.M. Masikhwa, N. Manyala, Examination of high-porosity activated carbon obtained from dehydration of white sugar for electrochemical capacitor applications, ACS Sustainable. Chem. Eng. 7 (2019) 537–546. https://doi.org/10.1021/acssuschemeng.8b04080.

[11] R. Yuan, H. Li, X. Yin, P. Wang, J. Lu, L. Zhang, Construction of multi-structures based on Cu NWs-supported MOF-derived Co oxides for asymmetric pseudocapacitors, J. Mater. Sci. Technol. 65 (2021) 182–189. https://doi.org/10.1016/j.jmst.2020.07.004.

[12] N.M. Ndiaye, M.J. Madito, B.D. Ngom, T.M. Masikhwa, A.A. Mirghni, N. Manyala, High-performance asymmetric supercapacitor based on vanadium dioxide and carbonized iron-polyaniline electrodes, AIP Adv. 9 (2019) 055309. https://doi.org/10.1063/1.5091799.

[13] A. Chandra, Supercapacitors: An alternate technology for energy storage, Proc. Natl. Acad. Sci. Sect. A Phys. Sci. 82 (2012) 79–90. https://doi.org/10.1007/s40010-012-0009-9.

[14] T. Lin, I.W. Chen, F. Liu, C. Yang, H. Bi, F. Xu, F. Huang, Nitrogen-doped mesoporous carbon of extraordinary capacitance for electrochemical energy storage, Science. 350 (2015) 1508–1513. https://doi.org/10.1126/science.aab3798.

[15] S. Yenisoy-Karakaş, A. Aygün, M. Güneş, E. Tahtasakal, Physical and chemical characteristics of polymer-based spherical activated carbon and its ability to adsorb organics, Carbon. 42 (2004) 477–484. https://doi.org/10.1016/j.carbon.2003.11.019.

[16] E. Raymundo-Piñero, F. Leroux, F. Béguin, A high-performance carbon for supercapacitors obtained by carbonization of a seaweed biopolymer, Adv. Mater. 18 (2006) 1877–1882. https://doi.org/10.1002/adma.200501905.

[17] H.G. Park, T.W. Kim, M.Y. Chae, I.K. Yoo, Activated carbon-containing alginate adsorbent for the simultaneous removal of heavy metals and toxic organics, Process Biochem. 42 (2007) 1371–1377. https://doi.org/10.1016/j.procbio.2007.06.016.

[18] L. Zhang, H. Gu, H. Sun, F. Cao, Y. Chen, G.Z. Chen, Molecular level one-step activation of agar to activated carbon for high performance supercapacitors, Carbon. 132 (2018) 573–579. https://doi.org/10.1016/j.carbon.2018.02.100.

[19] G. Makomaski, Porous structure and thermal properties of carbon adsorbents from pitch–polymer compositions, J. Therm. Anal. Calorim. 133 (2018) 1345–1352. https://doi.org/10.1007/s10973-018-7209-8.

[20] Z. Song, L. Miao, L. Ruhlmann, Y. Lv, D. Zhu, L. Li, L. Gan, M. Liu, Self-assembled carbon superstructures achieving ultra-stable and fast proton-coupled charge storage kinetics, Adv. Mater. 33 (2021) 2104148. https://doi.org/10.1002/adma.202104148.

[21] X. Zheng, L. Miao, Z. Song, W. Du, D. Zhu, Y. Lv, L. Li, L. Gan, M. Liu, In situ nanoarchitecturing of conjugated polyamide network-derived carbon cathodes toward high energy-power Zn-ion capacitors, J. Mater. Chem. A. 10 (2022) 611–621. https://doi.org/10.1039/d1ta07350h.

[22] S. Yan, C. Tang, H. Zhang, Z. Yang, X. Wang, C. Zhang, S. Liu, Free-standing cross-linked activated carbon nanofibers with nitrogen functionality for high-performance supercapacitors, Nanotechnology. 31 (2020) 025402. https://doi.org/10.1088/1361-6528/ab4536.

[23] B. Wang, J. Qiu, H. Feng, E. Sakai, T. Komiyama, Nitrogen doped carbon nanowires prepared from polypyrrole nanowires for potential application in supercapacitors, J. Electroanal. Chem. 775 (2016) 219–227. https://doi.org/10.1016/j.jelechem.2016.06.006.

[24] C. Xiong, B. Li, C. Duan, L. Dai, S. Nie, C. Qin, Y. Xu, Y. Ni, Carbonized wood cell chamber-reduced graphene oxide@PVA flexible conductive material for supercapacitor, strain sensing and moisture-electric generation applications, Chem. Eng. J. 418 (2021) 129518. https://doi.org/10.1016/j.cej.2021.129518.

[25] Y. Chen, X. Zhang, D. Zhang, P. Yu, Y. Ma, High performance supercapacitors based on reduced graphene oxide in aqueous and ionic liquid electrolytes, Carbon. 49 (2011) 573–580. https://doi.org/10.1016/j.carbon.2010.09.060.

[26] Y. Bai, R.B. Rakhi, W. Chen, H.N. Alshareef, Effect of pH-induced chemical modification of hydrothermally reduced graphene oxide on supercapacitor performance, J. Power Sources. 233 (2013) 313–319.

https://doi.org/10.1016/j.jpowsour.2013.01.122.

[27] N.M. Disa, K.S. Yuan, K.L. Tan, S. Tetsuo, The synthesized reduced graphene oxide enhanced the capacitive behavior of activated carbon/PVA as potential electrode materials, J. Nanostructures. 10 (2020) 296–306. https://doi.org/10.22052/jns.2020.02.009.

[28] H. Zhang, L. Lin, N. Hu, D. Yin, W. Zhu, S. Chen, S. Zhu, W. Yu, Y. Tian, Pillared carbon@tungsten decorated reduced graphene oxide film for pressure sensors with ultra-wide operation range in motion monitoring, Carbon. 189 (2021) 430–442. https://doi.org/10.1016/j.carbon.2021.12.080.

[29] J.M. Gohil, A. Bhattacharya, P. Ray, Studies on the cross-linking of poly(vinyl alcohol), J. Polym. Res. 13 (2006) 161–169. https://doi.org/10.1007/s10965-005-9023-9.

[30] S. Prasher, M. Kumar, S. Singh, Electrical and optical properties of O^{6+} ion beam-irradiated polymers, Int. J. Polym. Anal. Charact. 19 (2014) 204–211. https://doi.org/10.1080/1023666x.2014.879418.

[31] M. Li, X. Chang, X. Han, W. Yin, M. Ren, Resorcinol-formaldehyde resin based porous carbon materials with yolk-shell structure for high-performance supercapacitors, Synth. Met. 219 (2016) 67–75. https://doi.org/10.1016/j.synthmet.2016.05.011.

[32] X. Wang, J. Deng, X. Duan, D. Liu, J. Guo, P. Liu, Crosslinked polyaniline nanorods with improved electrochemical performance as electrode material for supercapacitors, J. Mater. Chem. A. 2 (2014) 12323–12329. https://doi.org/10.1039/c4ta02231a.

[33] L. Ding, H. Gao, F. Xie, W. Li, H. Bai, L. Li, Porosity-enhanced polymers from hyper-cross-linked polymer precursors, Macromolecules. 50 (2017) 956–962. https://doi.org/10.1021/acs.macromol.6b02715.

[34] F. Barzegar, V. Pavlenko, M. Zahid, A. Bello, X. Xia, N. Manyala, K.I. Ozoemena, Q. Abbas, Tuning the nanoporous structure of carbons derived from the composite of cross-linked polymers for charge storage applications, ACS Appl. Energy Mater. 4 (2021) 1763–1773. https://doi.org/10.1021/acsaem.0c02908.

[35] Y. Sun, G. Zhu, X. Zhao, W. Kang, M. Li, X. Zhang, H. Yang, L. Guo, B. Lin, Solution-processable, hypercrosslinked polymer via post-crosslinking for electrochromic supercapacitor with outstanding electrochemical stability, Sol. Energy Mater. Sol. Cells. 215 (2020) 110661. https://doi.org/10.1016/j.solmat.2020.110661.

[36] J. Pokharel, A. Gurung, A. Baniya, W. He, K. Chen, R. Pathak, B.S. Lamsal, N. Ghimire, Y. Zhou, MOF-derived hierarchical carbon network as an extremely-high-performance supercapacitor electrode, Electrochim. Acta. 394 (2021) 139058. https://doi.org/10.1016/j.electacta.2021.139058.

[37] M. Seo, S. Kim, J. Oh, S.-J. Kim, M.A. Hillmyer, Hierarchically porous polymers from hyper-cross-linked block polymer precursors, J. Am. Chem. Soc. 137 (2015) 600–603. https://doi.org/10.1021/ja511581w.

[38] T. Sharma, A. Joshi, A. Jain, K.R. Chaturvedi, Enhanced oil recovery and CO_2 sequestration potential of bi-polymer polyvinylpyrrolidone-polyvinyl alcohol, J. Pet. Sci. Eng. 211 (2022) 110167. https://doi.org/10.1016/j.petrol.2022.110167.

[39] T. Malik, H. Razzaq, S. Razzaque, H. Nawaz, A. Siddiqa, M. Siddiq, S. Qaisar, Design and synthesis of polymeric membranes using water-soluble pore formers: an overview, Polym. Bull. 76 (2018) 4879–4901. https://doi.org/10.1007/s00289-018-2616-3.

[40] G. Rivera-Hernández, M. Antunes-Ricardo, P. Martínez-Morales, M.L. Sánchez, Polyvinyl alcohol based-drug delivery systems for cancer treatment, Int. J. Pharm. 600 (2021) 120478. https://doi.org/10.1016/j.ijpharm.2021.120478.

[41] N.F. Sylla, N.M. Ndiaye, B.D. Ngom, D. Momodu, M.J. Madito, B.K. Mutuma, & N.

Manyala, Effect of porosity enhancing agents on the electrochemical performance of high-energy ultracapacitor electrodes derived from peanut shell waste, Sci. Rep. 9 (2019) 13673. https://doi.org/10.1038/s41598-019-50189-x.

[42] K.O. Oyedotun, M.J. Madito, A. Bello, D.Y. Momodu, A.A. Mirghni, N. Manyala, Investigation of graphene oxide nanogel and carbon nanorods as electrode for electrochemical supercapacitor, Electrochim. Acta. 245 (2017) 268–278. https://doi.org/10.1016/j.electacta.2017.05.150.

[43] J.G. Kim, H.C. Kim, N.D. Kim, M.S. Khil, N-doped hierarchical porous hollow carbon nanofibers based on PAN/PVP@SAN structure for high performance supercapacitor, Compos. Part B Eng. 186 (2020) 107825. https://doi.org/10.1016/j.compositesb.2020.107825.

[44] M. Rajesh, C.J. Raj, R. Manikandan, B.C. Kim, S.Y. Park, K.H. Yu, A high performance PEDOT/PEDOT symmetric supercapacitor by facile in-situ hydrothermal polymerization of PEDOT nanostructures on flexible carbon fibre cloth electrodes, Mater. Today Energy. 6 (2017) 96–104. https://doi.org/10.1016/j.mtener.2017.09.003.

[45] N.F. Sylla, S. Sarr, N.M. Ndiaye, B.K. Mutuma, A. Seck, B.D. Ngom, M. Chaker, N. Manyala, Enhanced electrochemical behavior of peanut-shell activated carbon/molybdenum oxide/molybdenum carbide ternary composites, nanomaterials. 11 (2021) 1056. https://doi.org/10.3390/nano11041056.

[46] O. Fasakin, J.K. Dangbegnon, D.Y. Momodu, M.J. Madito, K.O. Oyedotun, M.A. Eleruja, N. Manyala, Synthesis and characterization of porous carbon derived from activated banana peels with hierarchical porosity for improved electrochemical performance, Electrochim. Acta. 262 (2018) 187–196. https://doi.org/10.1016/j.electacta.2018.01.028.

[47] M.A. Pimenta, G. Dresselhaus, M.S. Dresselhaus, L.G. Cançado, A. Jorio, R. Saito,

Studying disorder in graphite-based systems by Raman spectroscopy, Phys. Chem. Chem. Phys. 9 (2007) 1276–1290. https://doi.org/10.1039/b613962k.

[48] A.C. Ferrari, J.C. Meyer, V. Scardaci, C. Casiraghi, M. Lazzeri, F. Mauri, S. Piscanec, D. Jiang, K.S. Novoselov, S. Roth, A.K. Geim, Raman spectrum of graphene and graphene layers, Phys. Rev. Lett. 97 (2006) 187401. https://doi.org/10.1103/phyrevlett.97.187401.

[49] M. Couzi, J.L. Bruneel, D. Talaga, L. Bokobza, A multi wavelength Raman scattering study of defective graphitic carbon materials: The first order Raman spectra revisited, Carbon. 107 (2016) 388–394. https://doi.org/10.1016/j.carbon.2016.06.017.

[50] A. Ghosh, A.M. da Silva Santos, J.R. Cunha, A. Dasgupta, K. Fujisawa, O.P. Ferreira, A.O. Lobo, M. Terrones, H. Terrones, B.C. Viana, CO_2 sensing by in-situ Raman spectroscopy using activated carbon generated from mesocarp of babassu coconut, Vib. Spectrosc. 98 (2018) 111–118. https://doi.org/10.1016/j.vibspec.2018.07.014.

[51] A. Sadezky, H. Muckenhuber, H. Grothe, R. Niessner, U. Pöschl, Raman microspectroscopy of soot and related carbonaceous materials: Spectral analysis and structural information, Carbon. 43 (2005) 1731–1742. https://doi.org/10.1016/j.carbon.2005.02.018.

[52] Y. Zhu, M. Chen, Y. zhang, W. Zhao, C. Wang, A biomass-derived nitrogen-doped porous carbon for high-energy supercapacitor, Carbon. 140 (2018) 404–412. https://doi.org/10.1016/j.carbon.2018.09.009.

[53] A. Bello, F. Barzegar, M.J. Madito, D.Y. Momodu, A.A. Khaleed, T.M. Masikhwa, J.K. Dangbegnon, N. Manyala, Stability studies of polypyrole- derived carbon based symmetric supercapacitor via potentiostatic floating test, Electrochim. Acta. 213 (2016) 107–114. https://doi.org/10.1016/j.electacta.2016.06.151.

[54] A.Y. Lee, K. Yang, N.D. Anh, C. Park, S.M. Lee, T.G. Lee, M.S. Jeong, Raman study

of D* band in graphene oxide and its correlation with reduction, Appl. Surf. Sci. 536 (2021) 147990. https://doi.org/10.1016/j.apsusc.2020.147990.

[55] S.S. Gunasekaran, S.K. Elumalali, T.K. Kumaresan, R. Meganathan, A. Ashok, V. Pawar, K. Vediappan, G. Ramasamy, S.Z. Karazhanov, K. Raman, R. Subashchandra Bose, Partially graphitic nanoporous activated carbon prepared from biomass for supercapacitor application, Mater. Lett. 218 (2018) 165–168. https://doi.org/10.1016/j.matlet.2018.01.172.

[56] T. Zhao, Z. Liu, X. Xin, H.M. Cheng, W. Ren, Defective graphene as a high-efficiency Raman enhancement substrate, J. Mater. Sci. Technol. 35 (2019) 1996–2002. https://doi.org/10.1016/j.jmst.2019.05.012.

[57] M.M. Rahman, M. Muttakin, A. Pal, A.Z. Shafiullah, B.B. Saha, A statistical approach to determine optimal models for IUPAC-classified adsorption isotherms, Energies. 12 (2019) 4565. https://doi.org/10.3390/en12234565.

[58] Q. Du, Y. Zhao, K. Zhuo, Y. Chen, L. Yang, C. Wang, J. Wang, 3D hierarchical porous carbon matching ionic liquid with ultrahigh specific surface area and appropriate porous distribution for supercapacitors, Nanoscale. 13 (2021) 13285–13293. https://doi.org/10.1039/d1nr01848e.

[59] Z. Zhou, L. Miao, H. Duan, Z. Wang, Y. Lv, W. Xiong, D. Zhu, L. Li, M. Liu, L. Gan, Highly active N, O-doped hierarchical porous carbons for high-energy supercapacitors, Chinese Chem. Lett. 31 (2020) 1226–1230. https://doi.org/10.1016/j.cclet.2020.02.026.

[60] Z. Song, L. Miao, L. Li, D. Zhu, Y. Lv, W. Xiong, H. Duan, Z. Wang, L. Gan, M. Liu, A universal strategy to obtain highly redox-active porous carbons for efficient energy storage, J. Mater. Chem. A. 8 (2020) 3717–3725. https://doi.org/10.1039/c9ta13520k.

[61] B. Wei, T. Wei, C. Xie, K. Li, F. Hang, Promising activated carbon derived from

sugarcane tip as electrode material for high-performance supercapacitors, RSC Adv. 11 (2021) 28138–28147. https://doi.org/10.1039/d1ra04143f.

[62] M. Mansuer, L. Miao, D. Zhu, H. Duan, Y. Lv, L. Li, M. Liu, L. Gan, Facile construction of highly redox active carbons with regular micropores and rod-like morphology towards high-energy supercapacitors, Mater. Chem. Front. 5 (2021) 3061–3072. https://doi.org/10.1039/d0qm01101k.

[63] P. Sonström, M. Bäumer, Supported colloidal nanoparticles in heterogeneous gas phase catalysis: On the way to tailored catalysts, Phys. Chem. Chem. Phys. 13 (2011) 19270–19284. https://doi.org/10.1039/c1cp22048a.

[64] S. Ma, J.J. Hou, H. Yang, Z. liang Xu, Preparation of renewable porous TiO_2/PVA composite sphere as photocatalyst for methyl orange degradation, J. Porous Mater. 25 (2018) 1071–1080. https://doi.org/10.1007/s10934-017-0518-7.

[65] J. Du, A. Chen, Y. Zhang, S. Zong, H. Wu, L. Liu, PVP-assisted preparation of nitrogen doped mesoporous carbon materials for supercapacitors, J. Mater. Sci. Technol. 58 (2020) 197–204. https://doi.org/10.1016/j.jmst.2020.02.088.

[66] T.S. He, X.D. Yu, T.J. Bai, X.Y. Li, Y.R. Fu, K. Di Cai, Porous carbon nanofibers derived from PAA-PVP electrospun fibers for supercapacitor, Ionics. 26 (2020) 4103–4111. https://doi.org/10.1007/s11581-020-03529-1.

[67] N.F. Sylla, N.M. Ndiaye, B.D. Ngom, B.K. Mutuma, D. Momodu, M. Chaker, N. Manyala, Ex-situ nitrogen-doped porous carbons as electrode materials for high performance supercapacitor, J. Colloid Interface Sci. 569 (2020) 332–345. https://doi.org/10.1016/j.jcis.2020.02.061.

[68] A. Khan, R.A. Senthil, J. Pan, S. Osman, Y. Sun, X. Shu, A new biomass derived rod-like porous carbon from tea-waste as inexpensive and sustainable energy material for advanced supercapacitor application, Electrochim. Acta. 335 (2020) 135588.

https://doi.org/10.1016/j.electacta.2019.135588.

[69] Y. Yang, S. Chen, L. Xu, Enhanced conductivity of polyaniline by conjugated crosslinking, Macromol. Rapid Commun. 32 (2011) 593–597. https://doi.org/10.1002/marc.201000806.

[70] S. Sundriyal, V. Shrivastav, H.D. Pham, S. Mishra, A. Deep, D.P. Dubal, Advances in bio-waste derived activated carbon for supercapacitors: Trends, challenges and prospective, Resour. Conserv. Recycl. 169 (2021) 105548. https://doi.org/10.1016/j.resconrec.2021.105548.

[71] N. Parveen, A.I. Al-Jaafari, J.I. Han, Robust cyclic stability and high-rate asymmetric supercapacitor based on orange peel-derived nitrogen-doped porous carbon and intercrossed interlinked urchin-like $NiCo_2O_4$@3DNF framework, Electrochim. Acta. 293 (2019) 84–96. https://doi.org/10.1016/j.electacta.2018.08.157.

[72] C. Liu, F. Li, M. Lai-Peng, H.M. Cheng, Advanced materials for energy storage, Adv. Mater. 22 (2010) E28–E62. https://doi.org/10.1002/adma.200903328.

[73] F. Barzegar, A.A. Khaleed, F.U. Ugbo, K.O. Oyeniran, D.Y. Momodu, A. Bello, J.K. Dangbegnon, N. Manyala, Cycling and floating performance of symmetric supercapacitor derived from coconut shell biomass, AIP Adv. 6 (2016) 115306. https://doi.org/10.1063/1.4967348.

[74] B. Moyo, D. Momodu, O. Fasakin, A. Bello, J. Dangbegnon, N. Manyala, Electrochemical analysis of nanoporous carbons derived from activation of polypyrrole for stable supercapacitors, J. Mater. Sci. 53 (2018) 5229–5241. https://doi.org/10.1007/s10853-017-1911-y.

[75] F. Barzegar, A. Bello, D. Momodu, M.J. Madito, J. Dangbegnon, N. Manyala, Preparation and characterization of porous carbon from expanded graphite for high energy density supercapacitor in aqueous electrolyte, J. Power Sources. 309 (2016)

245–253. https://doi.org/10.1016/j.jpowsour.2016.01.097.

[76] Y. Cheng, L. Huang, X. Xiao, B. Yao, L. Yuan, T. Li, Z. Hu, B. Wang, J. Wan, J. Zhou, Flexible and cross-linked N-doped carbon nanofiber network for high performance freestanding supercapacitor electrode, Nano Energy. 15 (2015) 66–74. https://doi.org/10.1016/j.nanoen.2015.04.007.